ORIGINAL RESEARCH **Open access**

Mapping Cotton Water Stress Variability Using UAV-Based Thermal Remote Sensing

Lucas Meyer[1*], Anna Schmidt[2], Stefan Braun[1], Laura Keller[3]

Abstract

Plant-based assessments, such as leaf water potential (LWP), are frequently used in irrigation scheduling because they are precise at signaling the need for water application. While highly effective, relying on LWP for scheduling proves labor-intensive and impractical for large areas. This research examined the viability of thermal remote sensing for evaluating cotton crop water status within the humid southeastern USA. The field trial spanned two growing seasons (2018 and 2020) in southwestern Georgia, U.S.A., employing a completely randomized block design with three irrigation levels (0% ETc (rainfed), 100% ETc (well-irrigated), and 125% ETc (over-irrigated)). Irrigation treatment impacts on cotton physiological responses were tracked by collecting predawn LWP (LWPPD), stomatal conductance (gs), and leaf area index (LAI) measurements across both seasons. Images acquired via UAV in the thermal infrared spectrum were used to derive the crop water stress index (CWSI) using three separate approaches, which were then tested as indicators of LWPPD. Outcomes revealed that LWPPD readings above -0.45 MPa indicate a non-stressed condition. In 2018, no detrimental effects were observed on leaf stomatal conductance or overall crop development. During 2020, lower and more erratic rainfall led to notable variations in LAI, gs, and LWPPD. Moderate to strong correlations emerged on every sampling date in 2020, particularly with the CWSI calculated via the Monteith method (CWSIMonteith), which recorded the two highest R2 values across the three dates (0.65 and 0.58) and the lowest RMSE values (0.02 and 0.04 MPa). In summary, the findings highlight the promise of a cost-effective UAV-based thermal setup for generating predicted LWP maps that reliably reflect field water conditions.

Keywords Cotton, UAV, Canopy temperature, Thermal images, Leaf water potential, Crop water stress index

*Correspondence:
Lucas Meyer
lucas.meyer@ethz.ch
[1] Department of AI for High-Altitude Vineyard Management, Faculty of Agriculture, ETH Zurich, Zurich, Switzerland
[2] Department of Machine Learning for Frost Protection Strategies, Faculty of Agriculture, University of Bern, Bern, Switzerland
[3] Department of Smart Soil Drainage Modeling, Faculty of Agriculture, EPFL Lausanne, Lausanne, Switzerland

Introduction

Cotton (*Gossypium hirsutum* L.) ranks as the leading fiber crop within worldwide commodity markets. It also holds major economic significance for the USA [1]. In 2021, nearly 4.5 million hectares were dedicated to cotton planting across the USA, delivering an average lint yield of 976 kg/ha, with most activity focused in the southern part of the nation [2]. Globally, cotton cultivation is primarily situated in semi-arid and arid zones, typically relying on irrigation, given the crop's sensitivity to surplus rainfall at key growth phases [3, 4] and its demand for intense sunlight and warmth [5]. Despite this concentration in dry climates, cotton adapts well to diverse water availability conditions [6, 7].

Within Georgia, typical rainfall totals during the cotton season generally satisfy the plant's water demands. Over the last 30 years, average rainfall from April through October has reached about 740 mm [8], whereas cotton requires

This is an open access article distributed under the terms of the Creative Commons Attribution-NonCommercial-ShareAlike 4.0 International License (CC BY-NC-SA 4.0), which permits non-commercial use, distribution, reproduction, and adaptation in any medium or format, provided that appropriate credit is given to the original author(s) and source, a link to the license is provided, and any changes made are indicated. Adapted material must be distributed under the same license.

© 2025 The Author(s). | Published by Agro Intelligence Research Press

approximately 457 mm to support strong yields in that location [9]. Still, rainfall patterns throughout the season often fail to coincide with periods of highest water uptake. Even brief agronomic drought periods at sensitive developmental points can lower floral bud counts, reduce boll retention [7], affect boll weight and spread [10], and diminish overall yield [11]. Drought conditions further reduce photosynthetic activity, partly through lowered stomatal conductance [12]. As a result, close to 50% of Georgia's cotton acreage receives irrigation. Excessive watering presents its own challenges by reducing irrigation efficiency due to drainage complications and causing yield declines [13]. Beyond that, surplus irrigation harms water supplies and can occasionally exhaust surface and groundwater reserves [14, 15].

Given the restrictions water deficits place on productivity, multiple irrigation scheduling strategies have emerged to refine application timing and volumes while raising water use efficiency [16-18]. Jones [19] grouped common scheduling techniques into three core categories: 1) soil water measurement involving decisions based on soil water potential and content, 2) soil water balance calculations that incorporate rainfall and evapotranspiration (ET) estimates, and 3) plant stress sensing, further split into tissue water status checks and physiological indicators. Leaf water potential (LWP) is an immediate measure of plant stress.

Measurements derived from the plant itself, including LWP, see broad application in irrigation scheduling [20-22] for their dependable alerts regarding irrigation timing. Despite occasional questions about LWP reliability stemming from short-term weather-driven shifts [19], studies have documented positive performance across several crops [23, 24]. For cotton specifically, Argyrokastritis *et al.* [25] evaluated LWP under full and deficit irrigation regimes, noting markedly lower values in stressed plants compared to well-watered ones, providing valuable data on water conditions and irrigation requirements. A 2016 investigation applied predawn LWP thresholds to initiate watering, yielding a 7-31% gain in water-use efficiency without sacrificing yields relative to the standard checkbook approach (weekly applications tied to crop growth stages) favored by producers [22].

Although a solid tool for guiding irrigation, Scholander pressure chamber measurements of LWP demand considerable time and are limited in coverage [26, 27], with each reading taking several minutes and requiring bulky gear. Consequently, investigators have pursued remote sensing options to identify or forecast crop water status as a substitute [28-30]. A prominent technique calculates the crop water stress index (CWSI) from canopy temperature data in thermal infrared imagery and links it to LWP [31]. Predictions of LWP derived this way have closely matched field measurements in dry settings and have supported mapping of spatial LWP differences [30].

Applying thermal infrared imagery for canopy temperature assessment presents greater difficulties in humid zones than in arid ones [32]. Isohydric crops commonly exhibit rising leaf temperatures under water deficit, as transpiration slows due to stomatal closure [33]. Yet leaf temperature also responds strongly to external variables, including relative humidity, air temperature, wind speed, and incoming radiation [34]. Humid settings feature reduced vapor pressure deficit (VPD), which narrows the temperature gap between stressed and unstressed plants because the surrounding air holds more moisture [33]. In addition, frequent partial cloudiness in such climates triggers swift temperature shifts within fields, hindering uniform imaging across entire areas [35].

This study aimed to assess the capability of a budget-friendly UAV thermal imaging platform for identifying water stress in cotton under the humid conditions of southern Georgia, where relative humidity stays above 80% during most of the season. The targeted objectives included 1) predicting LWPPD from UAV thermal images, 2) evaluating relationships among CWSI values produced by three alternative methods, and 3) illustrating how the CWSI/LWP connection can support the creation of meaningful predicted LWPPD field maps.

Materials and Methods

Study site and management practices

© 2025 The Author(s). | Published by Agro Intelligence Research Press

The experiment spanned two years, occurring in 2018 and 2020 at distinct research fields located at the University of Georgia's Stripling Irrigation Research Park (SIRP) near Camilla, GA **(Figure 1)**. During 2018, a total of 54 plots were prepared within a roughly 1 ha area (31°16′43.33 "N, 84°17′48.17 "W). Each plot contained 4 rows extending 12.2 m; only the middle 2 rows per plot provided data. Planting of three cultivars happened at a depth of 2.5 cm on May 2nd. These included PHY 330 and PHY 490 (PhytoGen, Dow AgroSciences LLC, IN) plus ST 6182 (GLT – Bayer Stoneville). The irrigation regimes applied were 0% ETc (crop evapotranspiration), 100% ETc, and 125% ETc. Researchers employed a randomized complete block design with 6 replicates per combination (3 varieties × 3 irrigation treatments × 6 replicates).

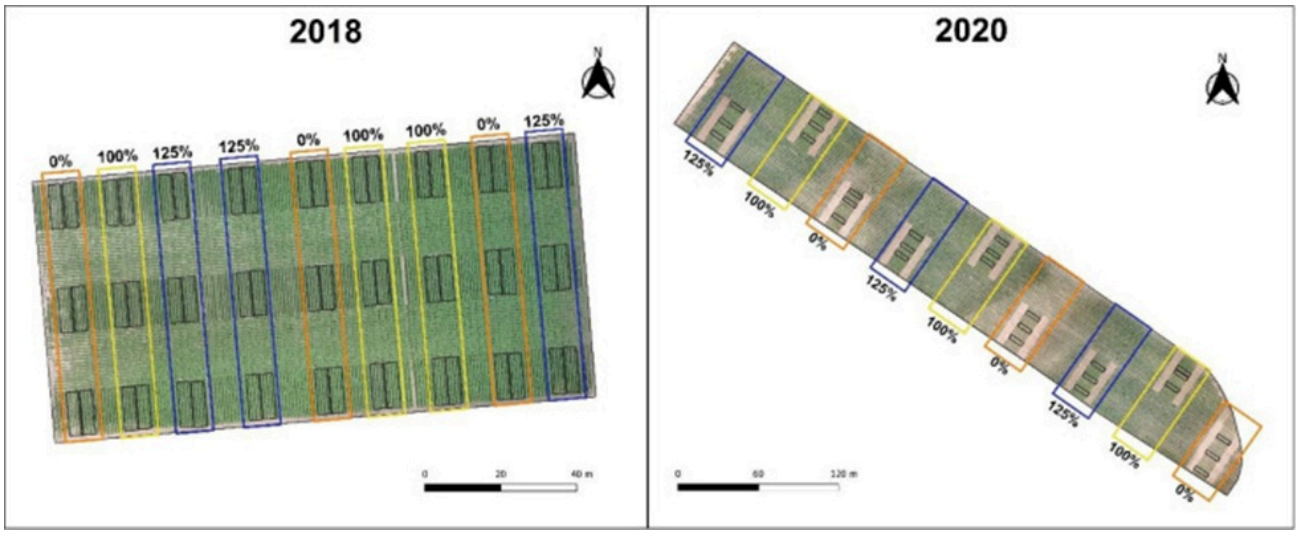

Figure 1. Layout of fields in 2018 and 2020. Irrigation treatments are shown in different colors. Well-watered treatment is represented as 100% ETc, and over-irrigated is represented as 125% ETc.

For 2020, 27 plots were prepared in a larger experimental field covering approximately 3.6 ha (31°16′58.88" N, 84°17′47.95" W). These plots kept the same dimensions as those used previously. Seeding with the DP 1646 (Deltapine, Bayer) cultivar occurred on May 13th. The same irrigation regimes from 2018 were repeated, this time alongside three plant growth regulator (PGR) applications. The PGR options included a control (no application), a moderate level (355 ml pix at first flower + 473 ml pix at 2 weeks), and an aggressive level (296 ml at 8 leaf + 355 ml at first flower + 2 weeks). A randomized complete block design included three replicates for every combination (3 irrigation treatments × 3 PGR treatments × 3 replicates).

Irrigation treatments

Delivery of the irrigation regimes used a linear move setup with overhead sprinklers during 2018, switching to three center pivot units in 2020. Both systems featured variable rate irrigation (VRI) capabilities. Daily ETc values came from the SmartIrrigation Cotton App [15]. This app derives ETc each day by combining reference ET (ET0) based on data from the nearby Camilla weather station (University of Georgia Weather Station Network), positioned less than 300 m away from the fields, together with a crop coefficient (Kc) taken from a curve tested for more than five years at SIRP [15]. Multiplying the daily Kc by the daily ET0 yielded the daily ETc figure. The 100% ETc regime matched the difference between daily ETc and rainfall, serving as the well-watered condition. For the 125% ETc regime, daily ETc minus precipitation was multiplied by 1.25 to calculate the applied volume, indicating the over-irrigated condition. Rainfed plots received water only until the squaring stage to assist early plant establishment, after which no additional irrigation was provided for the rest of the season. Irrigation events supplied 19.05 mm in 2018 and 20.3 mm in 2020. These quantities were chosen to minimize runoff risk and matched the overall capacity limits of the irrigation equipment.

Field data collection

© 2025 The Author(s). | Published by Agro Intelligence Research Press

Monitoring of irrigation treatment influences on cotton development and physiological activity involved gathering LWPPD, leaf area index (LAI), and stomatal conductance (gs) records across both years. Sampling extended from the squaring stage up to the final irrigation week. In 2018, this happened every week, but in 2020, it occurred every two weeks due to limited staff availability. Predawn LWP determinations took place from 04:00 to 06:00 h on the top fully expanded leaf from two plants inside each plot, utilizing a Scholander pressure chamber (Model 615; PMS Instruments, Albany, OR). Leaves were excised at the petiole base, enclosed in the chamber, and subjected to increasing pressure until xylem sap emerged at the cut end. Field LAI values were obtained with an AccuPAR LP-80 (Decagon Devices Inc., Pullman, WA) ceptometer. This instrument includes two linked light probes and a datalogger. One small quantum sensor on a tripod captured above-canopy photosynthetically active radiation (PAR), while a long probe fitted with several quantum sensors simultaneously recorded below-canopy PAR. Each plot received two paired readings: one with the extended probe running parallel to the rows and the other oriented perpendicular to the rows. Gas exchange data were also collected from the uppermost fully expanded leaf on two plants per plot. These readings were taken between 12:00 and 14:00 h using a LI-6800 (LI-COR Biosciences, Lincoln, NE) portable photosynthesis system. Settings inside the chamber maintained a reference CO2 concentration of 400 µmol mol−1, a flow rate of 600 µmol s−1, a light intensity of 1500 µmol m−2 s−1 of photosynthetically active radiation (PAR), a relative humidity of 60%, and an air temperature equal to ambient levels. Among all outputs, GS received the most focus for the current analysis.

UAV sensors and data acquisition

A 3DR Solo quadcopter (3D Robotics, Berkeley, CA, United States) fitted with a FLIR Vue Pro R (Model 640, 69° FOV, 9 mm, 30 Hz; FLIR Systems, Inc., Wilsonville, OR) camera gathered remote sensing information. Camera attachment used a rigid mount and a GPS geotagger (sUAS LLC, Beltsville, MD) to tag images mid-flight. The FLIR Vue Pro R uses an uncooled Vox microbolometer detector to capture 14-bit images (with built-in calibrated temperature readings) spanning the 7.5-13.5 µm wavelength range.

Acquisition of thermal imagery began at 65 days after planting (DAP), once canopy closure was sufficient to reduce soil background interference. The camera received a 15- to 20-minute warm-up period ahead of each flight. All missions happened within two hours of solar noon, specifically from 12:00 to 14:00 h. Flights in 2018 maintained a 50 m height at 4 m/s, with 80% overlap in both the frontal and side directions, resulting in a 10.5 cm spatial resolution for the thermal images. In 2020, the overlap percentages remained the same, yet altitude increased to 90 m and speed to 9 m/s to accommodate the expanded field size, yielding a spatial resolution of 16.5 cm that year.

Image processing

Stitching of the UAV images was performed in Pix4Dmapper (Pix4D SA, Lausanne, Switzerland) using a tailored template designed for maximum accuracy. Placement of ground control points (GCPs) at the four field corners improved geometric precision during this process. Field GPS receiver measurements supplied the GCP coordinates, which were subsequently loaded into the software. Each GCP was selected from at least 10 separate images to support calibration.

Thermal reflectance maps generated by Pix4Dmapper were then imported into ArcMap (ESRI, Redlands, CA, USA) for detailed processing and value extraction. Plot boundary shapefiles originated from the opening flight's imagery and functioned as the reference layer for aligning all later images, thereby decreasing row misalignment issues over time. An additional 0.5 m buffer strip surrounded each plot boundary. Together, these precautions prevented the extraction of pixels from neighboring rows outside the target plots.

Retrieval of canopy temperature followed the empirical technique presented by Meron *et al.* [36]. The approach assumes 1) that thermal image pixels belonging to canopy and soil can be divided according to upper and lower thresholds connected to air temperature, as expressed in **Eq. 1**:

© 2025 The Author(s). | Published by Agro Intelligence Research Press

$$(T_{air} - 10) < T_{cr} < (T_{air} + 7) \quad (1)$$

Where Tair is air temperature (°C), and Tcr is the temperature of canopy-related pixels in a thermal image, and 2) that the representative canopy temperature equals the average of the coolest 33% among the canopy pixels. This step discards mixed pixels, which are frequently located along row borders. Calculation of the final canopy temperature relies on the class-conditional histogram per **Eq. 2**.

$$T_c = \frac{\sum_{i=1}^{0.33n} T_{cr} * f_i}{\sum_{i=1}^{0.33n} f_i} \quad (2)$$

Where Tc (˚C) is the canopy temperature, fi is the number of pixels in each class cr of the histogram, and n is the number of pixels retained after the non-crop-related pixels were excluded.

Thermal camera accuracy

Evaluation of the temperature readings obtained from the FLIR Vue Pro R camera involved the construction of an inexpensive reference surface (RS) designed to mimic blackbody emissivity characteristics **(Figure 2)**. Objects classified as blackbodies have an emissivity value of 1, making them perfect radiators. The emissivity for any surface is the fraction of radiated energy it produces in comparison to a blackbody [37]. Construction of the RS used a 60 × 60 cm aluminum plate with a thickness of 2.2 cm. This dimension allowed the surfaces to occupy multiple pixels inside the thermal imagery. A matte paint with high emissivity covered one side of the plate. Attachment of four thin-film platinum resistance temperature detectors (RTDs) with three conductors to the underside of the plate enabled surface temperature monitoring. These Type A sensors have an accuracy rating of ± 0.15 °C. Real-time data acquisition was performed by an Arduino Mega embedded system (Arduino LLC, Torino, Italy) powered by rechargeable lithium batteries **(Figure 2a)**. The system was programmed to record at 5-second intervals. Linking the RTD sensors to the Arduino required an RTD sensor amplifier equipped with a MAX31865 breakout (Adafruit Industries, NY, USA) to preserve measurement precision. The four sensors were placed on the plate bottom, followed by a 25 mm layer of expanded polystyrene insulation foam **(Figure 2b)** to minimize air temperature interference and reduce large temperature swings within the plates. All electronic components were stored in a plastic project box for protection from sunlight and dust **(Figure 2c)**. The structural integrity of the full assembly (including the plate, insulation foam, and project box) was provided by a plastic pipe frame. The surfaces were positioned during flights at a central field spot to ensure visibility across many captured images **(Figures 2b and 2d)**.

© 2025 The Author(s). | Published by Agro Intelligence Research Press

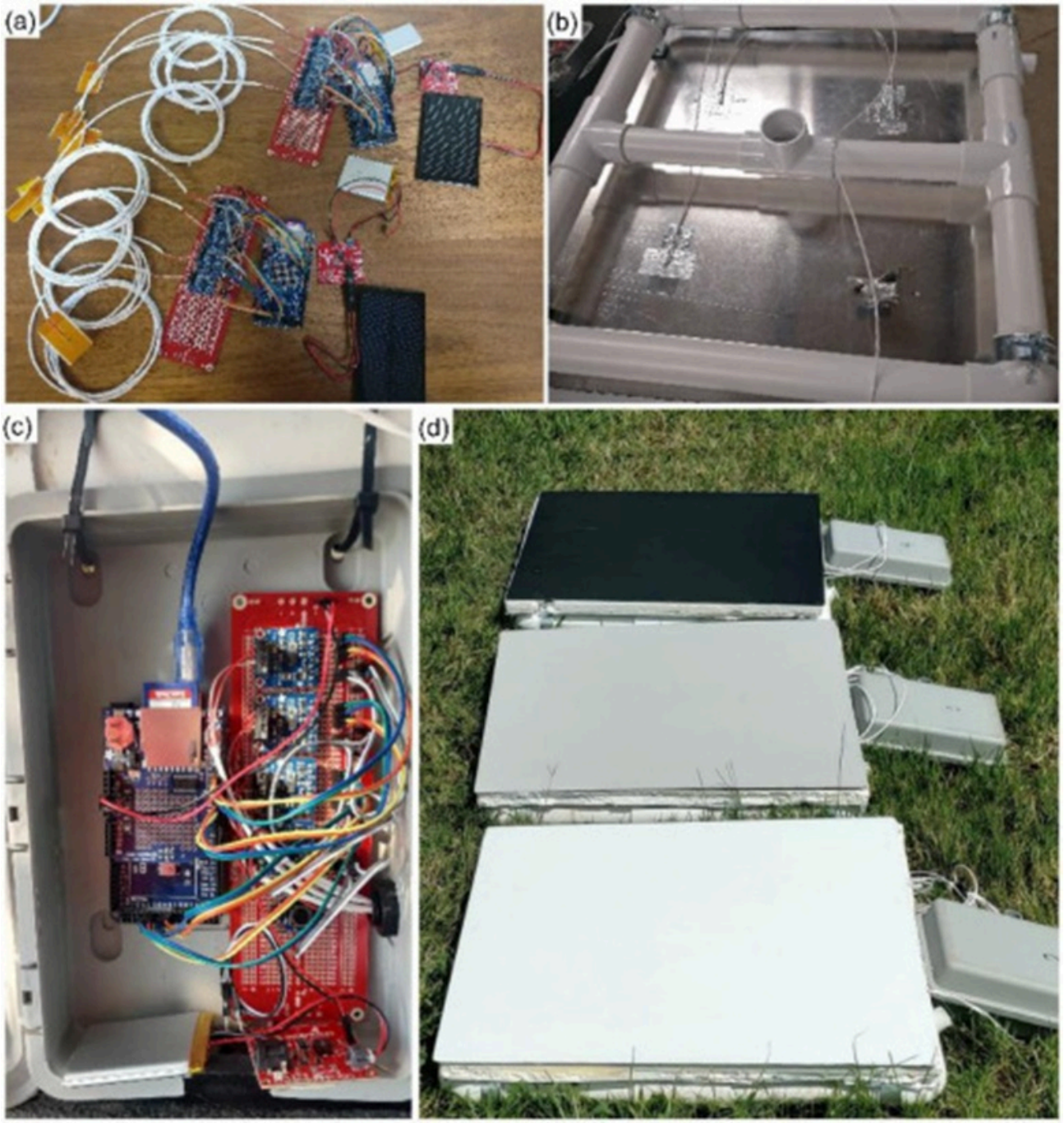

Figure 2. Electronics for temperature sensing in real time (a), placement of RTDs in the aluminum plate (b), electrical junction box with boards (c), and white, gray, and black RS in the field (d).

Three black-painted surfaces were deployed in the field for the 2018 thermal flights to check the reliability of extracted temperature information. In 2020, the modification of two surfaces with white and gray paint **(Figure 2c)** expanded the range of available reference temperatures. Calculating mean temperatures from the four RTD sensors allowed direct comparisons with the thermal camera outputs. Processing of separate images was performed using the ThermaCAM Researcher Pro 2.10 software (FLIR Systems, Inc., Wilsonville, OR). At least two images per flight, showing an RS aligned perpendicular to the camera view, underwent examination so pixel temperatures could be pulled for matching with averaged RTD readings. Alignment of timestamps guaranteed that measurements from each system corresponded to the same moments. Graphs comparing sensor temperatures with those from the FLIR camera showed close alignment

© 2025 The Author(s). | Published by Agro Intelligence Research Press

(Figure 3). Recorded errors reached +1.54 °C in 2018 and +2.18 °C in 2020, indicating a slight overestimation in the image-based temperatures. Nevertheless, these deviations remained within the expected ±5 °C tolerance for sensors of this category.

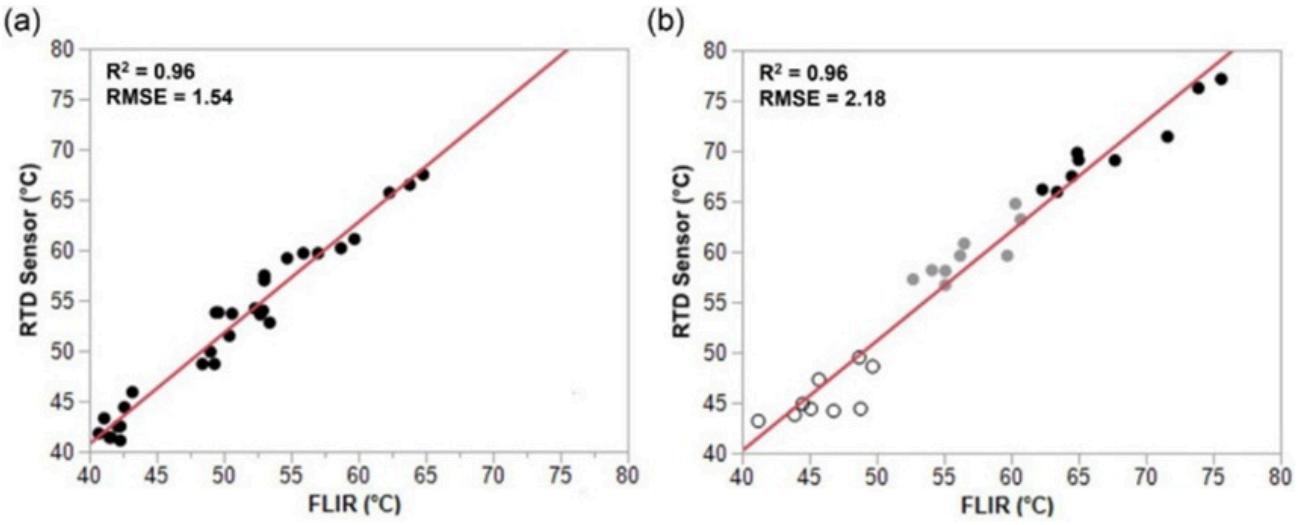

Figure 3. Comparison between FLIR-based temperature and RTD sensor temperature in (a) 2018 and (b) 2020. White, grey, and black points in 2020 refer to the different colored surfaces.

Crop water stress index

UAV thermal camera canopy temperature records enabled CWSI computation through the expression CWSI= (Tc – Twet) / (Tdry – Twet). In this scale, CWSI extends from 0 (fully unrestricted water availability) to 1 (complete cessation of transpiration) [38]. Here, Twet stands for the temperature belonging to a leaf with unrestricted transpiration activity, while Tdry represents a leaf without any transpiration. Determination of the wet and dry baseline values followed three distinct procedures. The initial CWSI version (CWSIJones1) drew upon theoretical baselines for both wet and dry conditions, based on the energy balance relation outlined by Jones [39]. In the next version (CWSIJones2), the theoretical wet baseline remained unchanged, but an empirical dry baseline emerged at 5 °C above the air temperature. The final version (CWSIMonteith) incorporated a theoretical wet baseline from Monteith and Unsworth [40] and the identical empirical dry baseline used in CWSIJones2. All baseline derivations utilized meteorological inputs sourced from the Camilla weather station. Averaging of readings logged at 15-minute intervals between 12:00 and 14:00 h formed the dataset for computations. The Tc component in the CWSI formula was the mean temperature of the 33% coolest pixels within each plot.

Statistical analysis

Assessment of irrigation treatment influences (as the between-subject element) across multiple time intervals (as the within-subject element) applied a two-way mixed analysis of variance (ANOVA) via the rstatix package running in R 4.1.0 (R Foundation for Statistical Computing, Vienna, Austria). Follow-up comparisons of treatment averages used the Bonferroni test. Data for LAI, LWPPD, and gs analysis were included for every irrigation and cultivar combination from 2018 and for all irrigation and PGR combinations from 2020. Examination of links between the three CWSI variants and LWPPD employed second-order polynomial regression models. Judgment of predictive performance for each CWSI against LWPPD relied on the coefficient of determination (R2) and the root mean square error (RMSE). The particular CWSI approach offering the largest R2 value paired with the smallest RMSE (MPa) supported the mapping demonstration of predicted LWPPD from thermal imagery. RMSE values were calculated using **Eq. 3**.

© 2025 The Author(s). | Published by Agro Intelligence Research Press

$$RMSE = \sqrt{\frac{1}{n} x \sum_{i=1}^{n} (Pi - Oi)^2} \quad (3)$$

Where n is the number of samples, and Pi and Oi represent the predicted and observed values.

Results and Discussion

Weather and Irrigation

Minimum along with maximum air temperatures and precipitation patterns for the two growing seasons appear illustrated in **Figure 4**. The 2018 season experienced abundant rainfall, including monthly averages over 100 mm for May and June plus levels exceeding 200 mm in mid-season, while 2020 presented lighter early rainfall followed by heavier amounts in August and September. Overall water supply (rainfall + irrigation) for each treatment during 2018 surpassed the 2020 total by more than 1.5 times, largely due to elevated precipitation **(Table 1)**. Production of cotton in Georgia generally requires nearly 460 mm of water, distributed evenly across developmental phases [9, 41]. Precipitation totals in 2018 greatly exceeded this cotton requirement, but 2020 fell short by approximately 113 mm.

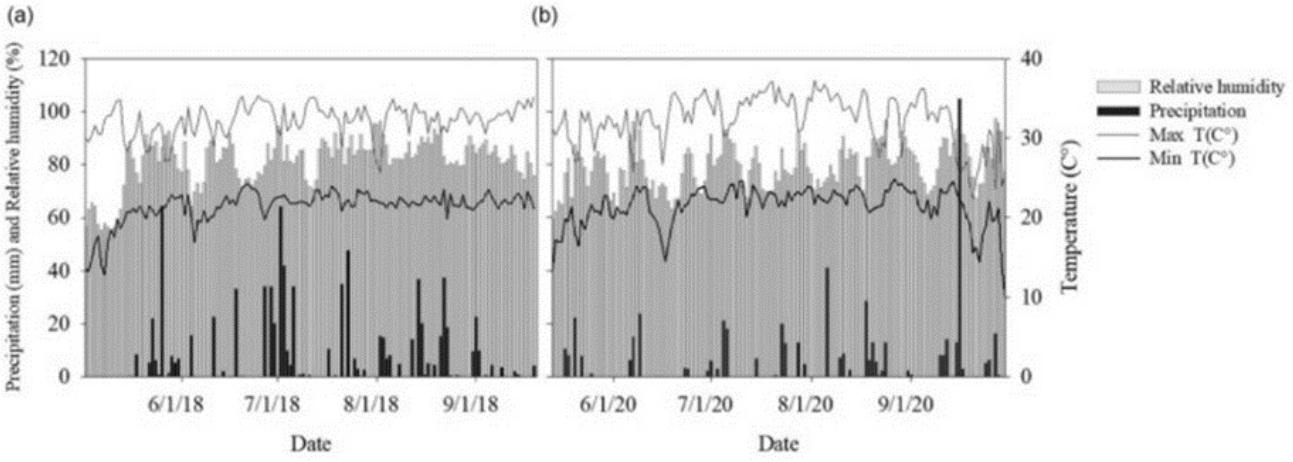

Figure 4. Daily precipitation, relative humidity (%) and maximum and minimum air temperatures during the cotton growing season in 2018 (a) and 2020 (b).

Table 1. Irrigation, rainfall, and total water applied in both fields in Camilla, GA, during the 2018 and 2020 growing seasons.

Year	Treatment	Total water (mm)	Precipitation (mm)	Irrigation (mm)
2018	Rainfed	828	828	0
	100% ET_c	1048	828	220
	125% ET_c	1079	828	251
2020	Rainfed	383	347	36
	100% ET_c	599	347	252
	125% ET_c	656	347	309

© 2025 The Author(s). | Published by Agro Intelligence Research Press

Daily cotton water needs in humid climates average about 2.54 mm from emergence through first square [42, 43]. Between the first square and the first flower, this daily amount shifts into the 2.54 to 5.08 mm range, climbing further to a maximum from early flowering into peak bloom, where daily usage advances from 5.08 to 7.11 mm. Plants display notable sensitivity to water shortages at squaring [42], with resulting drought restricting overall size and node development [44], though vulnerability peaks sharply in early bloom. Brief drought episodes then become especially harmful, affecting both yield output and fiber quality. Water consumption per day declines after peak bloom, yet moderate sensitivity to deficits persists. Better rainfall timing in 2018 ensured sufficient water availability through every growth phase. The opposite pattern in 2020, characterized by reduced and irregular rainfall, led to short drought spells in the rainfed areas. Extended rain-free stretches lowered average daily precipitation to 0.86 mm across the squaring window, well below required levels. Similarly, a 17-day interval in early bloom accumulated just 7.87 mm of total precipitation.

Leaf area index (LAI)

Averages for LAI across treatments are shown in **Figure 5**. Comparable seasonal progressions occurred in both years, beginning with modest values near 1 between 36 and 50 DAP during early growth, followed by swift canopy expansion from 50 to 80 DAP, and then a gradual reduction toward season's end. Cotton crops typically exhibit this rise-and-fall curve from early flowering into open boll regardless of the moisture regime [45]. Heavy rainfall throughout 2018 generated nearly identical LAI figures for all irrigation regimes, showing no meaningful statistical separation on any measurement date **(Figure 5a)**. In 2020, however, clear distinctions emerged between rainfed and irrigated plots on every date except 38 DAP **(Figure 5b)**. Uniform early irrigation across treatments supported consistent establishment and initial development.

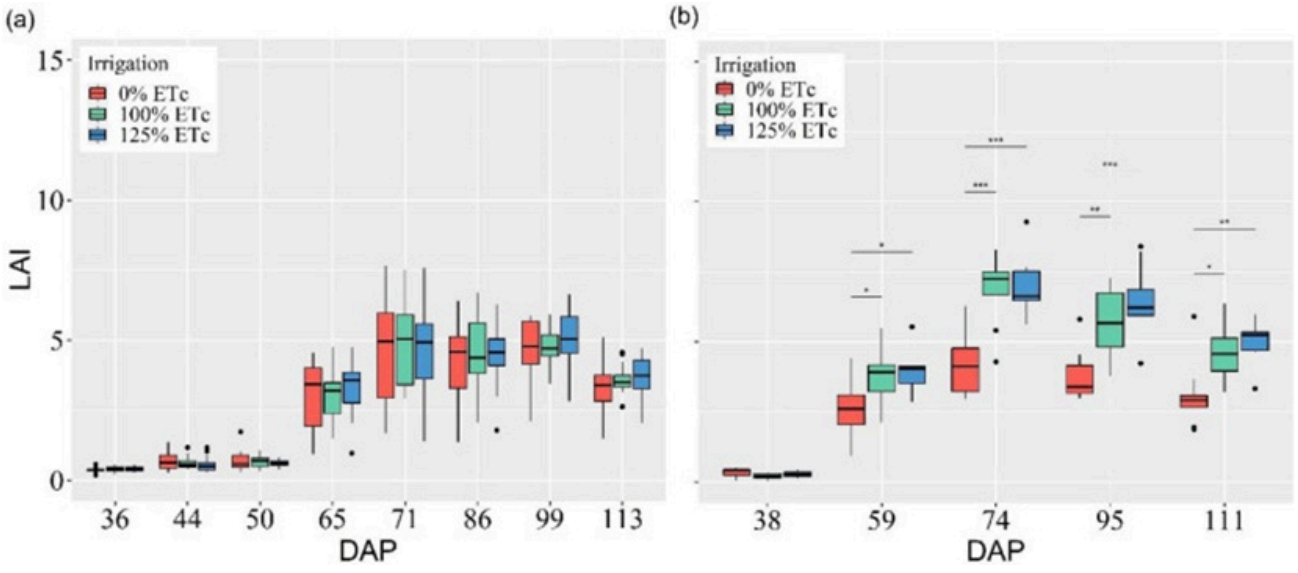

Figure 5. Leaf area index (LAI) treatment averages and seasonal trends in Camila, GA, in 2018 (a) and 2020 (b). The two-way mixed ANOVA results are shown in the figures as follows: $P < 0.05$, $P < 0.01$, and $P < 0.001$. Data represent means ± SE (2018; $n = 18$, 2020; $n = 9$).

The maximum average LAI values for the 2020 treatments occurred at 74 DAP: 6.99 for 125% ETc, 6.79 for 100% ETc, and 4.26 for 0% ETc. The rainfed regime consistently produced the smallest weekly means, ranging from 38 to 45% below well-watered levels and 44 to 51% below over-irrigated levels. The largest treatment separations occurred at peak flowering, coinciding with the highest overall LAI. Well-watered and over-irrigated plots maintained parallel development with no detectable differences at any stage. Analogous responses of cotton LAI to varying irrigation intensities were reported by Noreen *et al.* [46]. Drought impacts on the rainfed regime proved most pronounced at peak flowering, where LAI reached maximums and treatment contrasts became clearest.

© 2025 The Author(s). | Published by Agro Intelligence Research Press

As a vital morphological feature, leaf area strongly governs crop ET rates [47] and directly influences harvest yield [48]. Drought conditions readily impair this trait by interfering with cell division and cell enlargement [49, 50]. Work by Noreen *et al.* [46] identified a robust association between LAI and final boll weight (r = 0.77) when water supply remained adequate. This relationship intensified markedly during drought (r = 0.95), reinforcing the idea that LAI decline due to water limitation is a primary driver of reduced final productivity.

Predawn Leaf water potential (LWPPD) and stomatal conductance (gs)

Seasonal weekly trends of LWPPD and gs across both growing seasons are displayed in **Figure 6**. In 2018, notable differences in LWPPD among the irrigation treatments appeared in 6 of the 8 sampling dates assessed **(Figure 6a)**. At 36 and 65 DAP, the 125% ETc treatment recorded the highest LWPPD values, whereas after 71 DAP the 0% ETc (dryland) treatment consistently showed the highest values. Even with these variations among irrigation treatments, the measured LWPPD stayed relatively elevated throughout the entire season. The highest and lowest weekly LWPPD averages for the season were -0.21 and -0.45 MPa, both recorded under the 125% ETc treatment. This narrow range of LWPPD suggests that the plants did not experience significant water stress, largely due to abundant rainfall that year. This lack of stress is further evident in the weekly gs averages across treatments **(Figure 6b)**. No meaningful differences in average gs were found among irrigation treatments in 2018. The lowest and highest gs values occurred in the 125% ETc treatment at 86 DAP (0.57 mmol H2O m−2s−1) and at 44 DAP (1.79 mmol H2O m−2s−1), respectively.

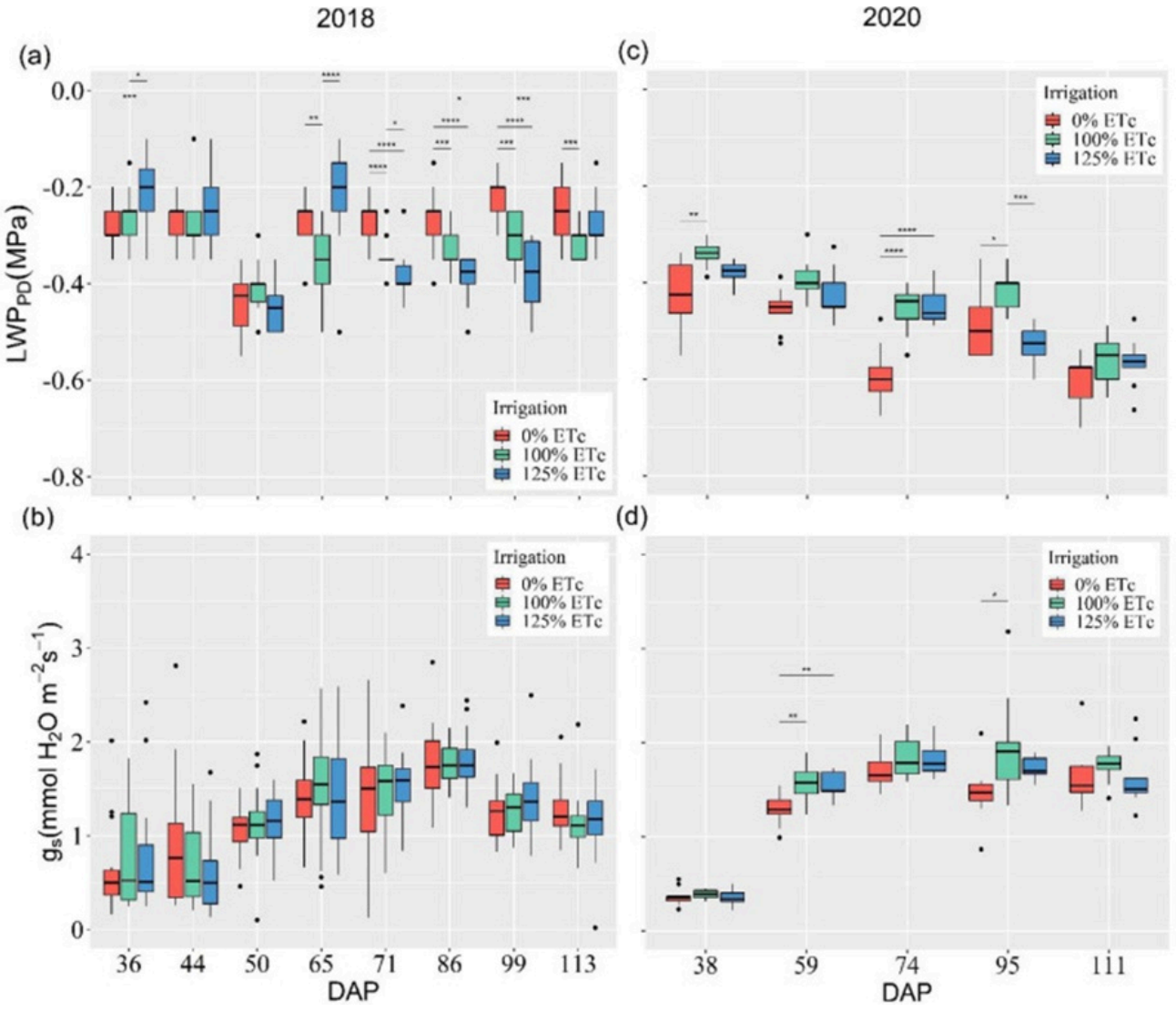

© 2025 The Author(s). | Published by Agro Intelligence Research Press

Figure 6. Predawn leaf water potential (LWPPD) expressed in MPa (a,c) and stomatal conductance (gs) expressed in mmol H2O m−2s−1 (b,d) treatment averages and seasonal trends for three different irrigation treatments during the 2018 and 2020 growing seasons. The 2018 growing season is represented on the left panel and the 2020 growing season on the right panel. The two-way mixed ANOVA results are represented in the figures as follows: P < 0.05, P < 0.01, P < 0.001, P < 0.0001. Data represent means ± SE (2018; n = 18, 2020; n = 9).

During the 2020 growing season, weekly LWPPD averages across irrigation treatments differed significantly on three occasions **(Figure 6c)**. Rainfed treatment averages differed markedly from the well-watered treatment at 38 DAP (P < 0.001), 74 DAP (P < 0.0001), and 95 DAP (P < 0.05). The over-irrigated treatment differed from rainfed at 74 DAP (P < 0.0001), and well-watered differed from over-irrigated at 95 DAP (P < 0.001). The highest seasonal average LWPPD was recorded in the well-watered treatment (-0.34 MPa), followed by the over-irrigated treatment (-0.37 MPa). The lowest weekly LWPPD average occurred in the rainfed treatment (-0.6 MPa). Rainfed plots exhibited an average LWPPD that was 16% lower than the 100% ETc treatment. This decline in LWPPD results from the isohydric response of cotton plants [1, 51], in which leaf water potential decreases as soil water potential declines.

As noted earlier, canopy development was markedly reduced in the rainfed plots, resulting in lower LAI than in the irrigated treatments in 2020. Chastain *et al.* [22] reported that plant growth suppression occurs only when LWPPD falls below -0.8 MPa. Although the measured LWPPD values in the second season remained above this threshold, more intense drought periods occurred between measurement dates. Even though these low-precipitation intervals did not coincide with LWPPD sampling days, their impact was clearly evident in the rainfed plots, as evidenced by differences in leaf area between the rainfed and irrigated treatments.

Stomatal conductance (gs) treatment averages showed statistical differences on two occasions in the 2020 growing season **(Figure 6d)**. The rainfed treatment gs average was substantially lower than both the well-watered and over-irrigated treatments (P < 0.0001) at 59 DAP, and lower than the well-watered treatment (P < 0.05) at 95 DAP, while the two irrigated treatments differed significantly (P < 0.001) only at 95 DAP. Consistent with LWPPD patterns, gs averages were lower in the rainfed plots. The well-watered and over-irrigated treatments maintained comparable average gs levels across the season with no significant differences.

The decline in leaf stomatal conductance represents a typical adaptation in drought-stressed plants aimed at reducing water loss [52]. Lower leaf water potential occurs as soil water availability diminishes, prompting stomatal closure [53]. In the same study, a major drop in gs was observed 3 days after drought exposure. A recent study reported that gs in rainfed plots was 72 and 58% lower than in irrigated treatments across two successive years [1]. Pilon *et al.* [53] documented even larger differences reaching 81% between well-watered and drought-stressed cotton plants.

Crop water stress index (CWSI)

Figure 7 illustrates the weekly CWSI values for treatment derived from the three distinct methodologies. All approaches produced comparable seasonal patterns in both years. In 2018, no significant differences appeared in treatment CWSI averages across any of the observed dates **(Figures 7a-7c)**. The 100% ETc treatment displayed the lowest CWSI values throughout the season, ranging from 0.23 to 0.37 for CWSIJones1, CWSIMonteith, and CWSIJones2, respectively. The highest stress level using the CWSIJones1 method was 0.5, recorded for the 100% ETc treatment at 65 DAP, while for CWSIMonteith and CWSIJones2 the peak stress indices occurred in the 0% ETc treatment at 113 DAP (0.78 and 0.76, respectively).

© 2025 The Author(s). | Published by Agro Intelligence Research Press

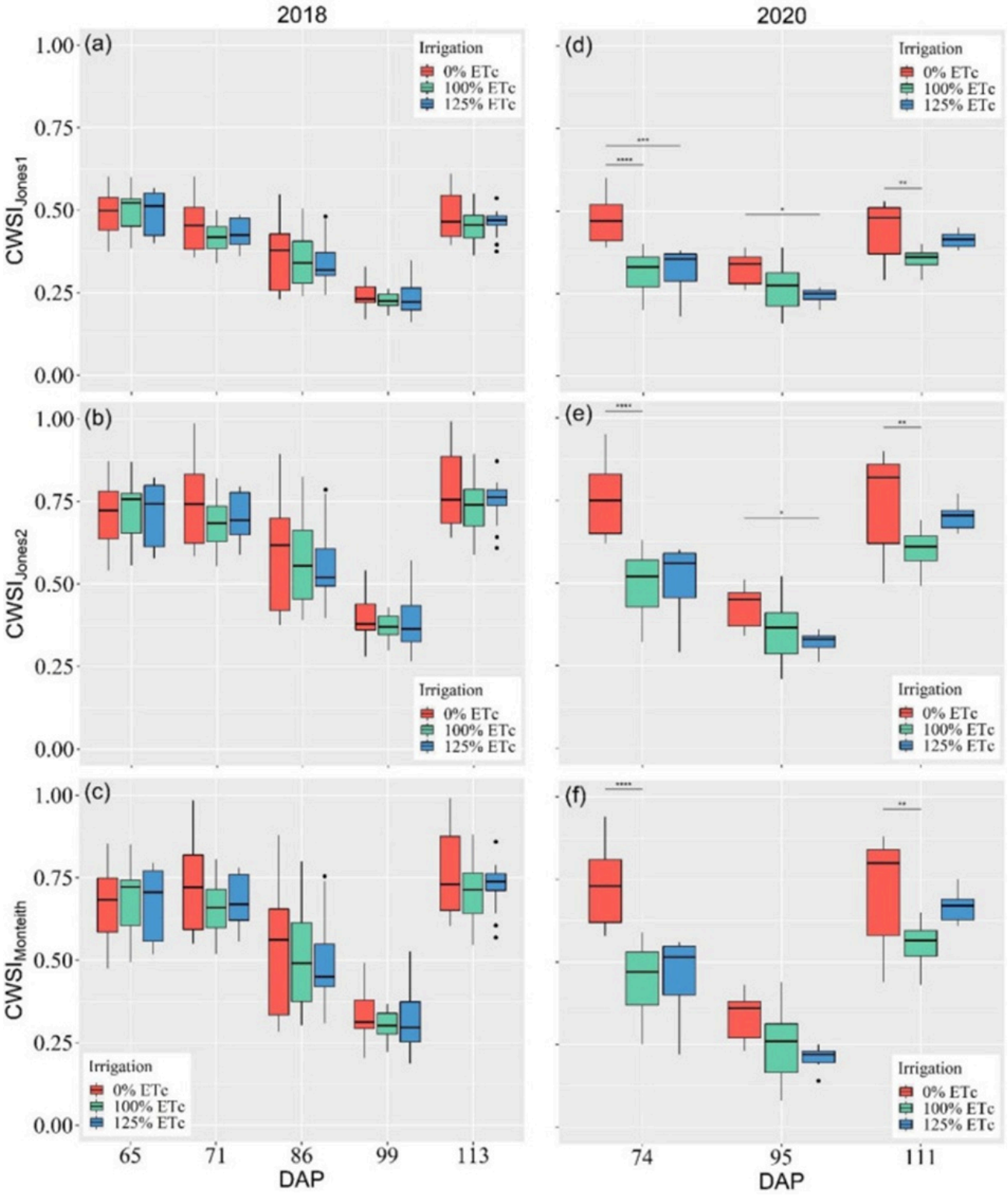

Figure 7. Crop water stress index (CWSI) approaches treatment averages and seasonal trends for three different irrigation treatments during the 2018 and 2020 growing seasons. The 2018 growing season is represented on the left panel and the 2020 growing season on the right panel. The two-way mixed ANOVA results are represented in the figures as follows: $P < 0.05$, $P < 0.01$, $P < 0.001$, $P < 0.0001$. Data represent means ± SE (2018; n = 18, 2020; n = 9).

© 2025 The Author(s). | Published by Agro Intelligence Research Press

In 2020, CWSI treatment averages differed significantly on every date for the Jones 1 and Jones 2 methods and on two dates (74 and 111 DAP) for the Monteith equation **(Figures 7d-7f)**. Rainfed plots registered significantly higher CWSI values than the 100% ETc treatment for all CWSI calculations at 74 DAP ($P < 0.0001$) and at 111 DAP ($P < 0.01$). Rainfed and 125% ETc treatments showed significant differences for Jones 1 and Jones 2 at 95 DAP ($P < 0.05$) and for Jones 1 at 74 DAP ($P < 0.001$). Across both seasons, CWSIJones1, based on theoretical dry and wet baselines, generally produced lower values than the Jones 2 and Monteith methods, which rely on an empirical dry baseline. These variations stem from constraints inherent in the energy balance model employed in the theoretical method. Energy balance models depend on the traits of a hypothetical leaf representing typical leaf characteristics, assuming equilibrium with the surrounding environment [28]. Deviations from these assumed parameters can lead to errors, resulting in the dry baseline being either higher or lower than empirically obtained values.

Simple regression models for cotton LWPPD prediction

CWSI/LWPPD models were built for each of the three CWSI methods across 5 separate dates in 2018 and 3 dates in 2020. **Table 2** displays the equations and performance metrics for each model. Performance assessment relied on R2 and RMSE values.

Table 2. Regression models between CWSI and LWPPD on different dates in 2018 and 2020.

Year	DAP	CWSI method	Equation	RMSE (MPa)	R^2
2018	**65**	Jones 1	$y = -0.198x^2 - 0.302x - 0.124$	0.05	0.37
		Jones 2	$y = -0.268x^2 - 0.018x - 0.175$	0.05	0.38
		Monteith	$y = -0.222x^2 - 0.057x - 0.186$	0.05	0.38
	71	Jones 1	$y = 2.388x^2 - 1.761x - 0.163$	0.04	0.47
		Jones 2	$y = 0.729x^2 - 0.308x - 0.565$	0.04	0.43
		Monteith	$y = 0.544x^2 - 0.091x - 0.598$	0.04	0.43
	86	Jones 1	$y = -9.999x^2 + 6.294x - 1.301$	0.04	0.35
		Jones 2	$y = -6.218x^2 + 4.879x - 1.268$	0.04	0.34
		Monteith	$y = -4.020x^2 + 2.004x - 0.560$	0.04	0.33
	99	Jones 1	$y = -7.202x^2 + 5.726x - 1.425$	0.06	0.09
		Jones 2	$y = -5.637x^2 + 4.549x - 1.205$	0.06	0.08
		Monteith	$y = -3.398x^2 + 1.722x - 0.506$	0.06	0.08
	113	Jones 1	$y = 9.132x^2 - 8.461x + 1.672$	0.03	0.15
		Jones 2	$y = 2.004x^2 - 2.843x + 0.723$	0.03	0.04
		Monteith	$y = 3.138x^2 - 4.177x + 1.102$	0.03	0.15

© 2025 The Author(s). | Published by Agro Intelligence Research Press

2020	**74**	Jones 1	$y = 0.348x^2 - 0.789x - 0.258$	0.04	0.57
		Jones 2	$y = 0.144x^2 - 0.504x - 0.256$	0.04	0.57
		Monteith	$y = 0.105x^2 - 0.420x - 0.304$	0.04	0.58
	95	Jones 1	$y = 9.483x^2 - 4.832x + 0.101$	0.04	0.46
		Jones 2	$y = 5.136x^2 - 3.410x + 0.052$	0.04	0.44
		Monteith	$y = 3.795x^2 - 1.672x - 0.330$	0.04	0.45
	111	Jones 1	$y = -7.5207x^2 + 5.9x - 1.7061$	0.02	0.65
		Jones 2	$y = -2.6216x^2 + 3.4957x - 1.7137$	0.02	0.65
		Monteith	$y = -2.1493x^2 + 2.6977x - 1.3949$	0.02	0.65

In 2018, the prediction models exhibited weak to moderate associations between CWSI and LWPPD, likely because water status varied little across plots. The strongest associations occurred at 71 DAP, with R2 values of 0.47, 0.43, and 0.43 for CWSIJones1, CWSIJones2, and CWSIMonteith, respectively. These were followed by models at 65 DAP (average R2 = 0.38) and at 86 DAP (average R2 = 0.34). The weakest R2 values occurred at 99 DAP, ranging from 0.08 for CWSIJones2 and CWSIMonteith to 0.09 for CWSIJones1. The highest RMSE values also occurred at 99 DAP, with a value of 0.06 MPa across all 3 methods. In general, prediction errors stayed fairly low, fluctuating between 0.03 and 0.06 across all dates. The top-performing model on each date relied on CWSIJones1, delivering marginally higher R2 values, except at 65 DAP, where CWSIJones2 and CWSIMonteith achieved slightly higher R2 values.

In 2020, every CWSI demonstrated moderate to strong nonlinear associations with LWPPD. Top models occurred at 111 DAP, attaining R2 values of 0.65 and RMSEs of 0.02 MPa across all three CWSIs. At 74 DAP, the prediction models reached R2 values of 0.57 for both CWSIJones1 and CWSIJones2, and 0.58 for CWSIMonteith, with an error of 0.04 MPa. Performance dropped at 95 DAP, with R2 values of 0.46, 0.44, and 0.45 for CWSIJones1, CWSIJones2, and CWSIMonteith, respectively, and an RMSE of 0.04 across all three methods. Model outcomes remained highly comparable during the second season. CWSIJones1 produced a marginally higher R2 at 74 DAP, while CWSIMonteith performed marginally better at 95 DAP.

Chastain *et al.* [22] first established the relationship between CWSI and LWPPD in the southeastern US through a 2016 study in the same region, using in-field infrared proximal canopy temperature sensors. That work also identified a nonlinear link with a coefficient of determination reaching 0.93. The 2016 results revealed broader LWPPD variation. Unlike the Chastain *et al.* [22] study, CWSI values here are derived from UAV-based sensors capturing temperature across entire plot areas, yet still produced moderate to relatively strong associations on chosen dates even with reduced LWPPD variation. CWSI calculations for plots showing higher LWPPD were generally higher than those reported by Chastain *et al.* [22], suggesting that UAV camera canopy temperature readings overestimated values relative to proximal infrared sensors.

Findings from this research, which applied both empirical and theoretical baselines, together with those of Chastain *et al.* [22], who used empirical wet- and dry-season baselines from Idso [38], pointed to a nonlinear relationship between CWSI and LWP in the humid Southeast of the USA. Alchanatis *et al.* [28] established the CWSI/LWP link for cotton through empirical and theoretical baselines and identified a strong linear association. Their research took place in Israel, under a Mediterranean climate with low humidity during the growing season. Comparable linear patterns also emerged in the arid

© 2025 The Author(s). | Published by Agro Intelligence Research Press

setting of northwestern Texas, USA, with empirical CWSI [54]. These outcomes imply that connections between varied CWSI approaches and LWPPD depend heavily on the specific region and must account for distinct environmental factors.

Weekly models achieving R2 above 0.5 served as the basis for generating predicted LWPPD maps. The CWSIMonteith-based model was selected for use because it delivered the highest R2 among approaches at 74 DAP. The CWSIMonteith/LWPPD equations were applied to UAV images at 74 and 111 DAP, yielding the two predicted LWPPD maps shown in **Figure 8**.

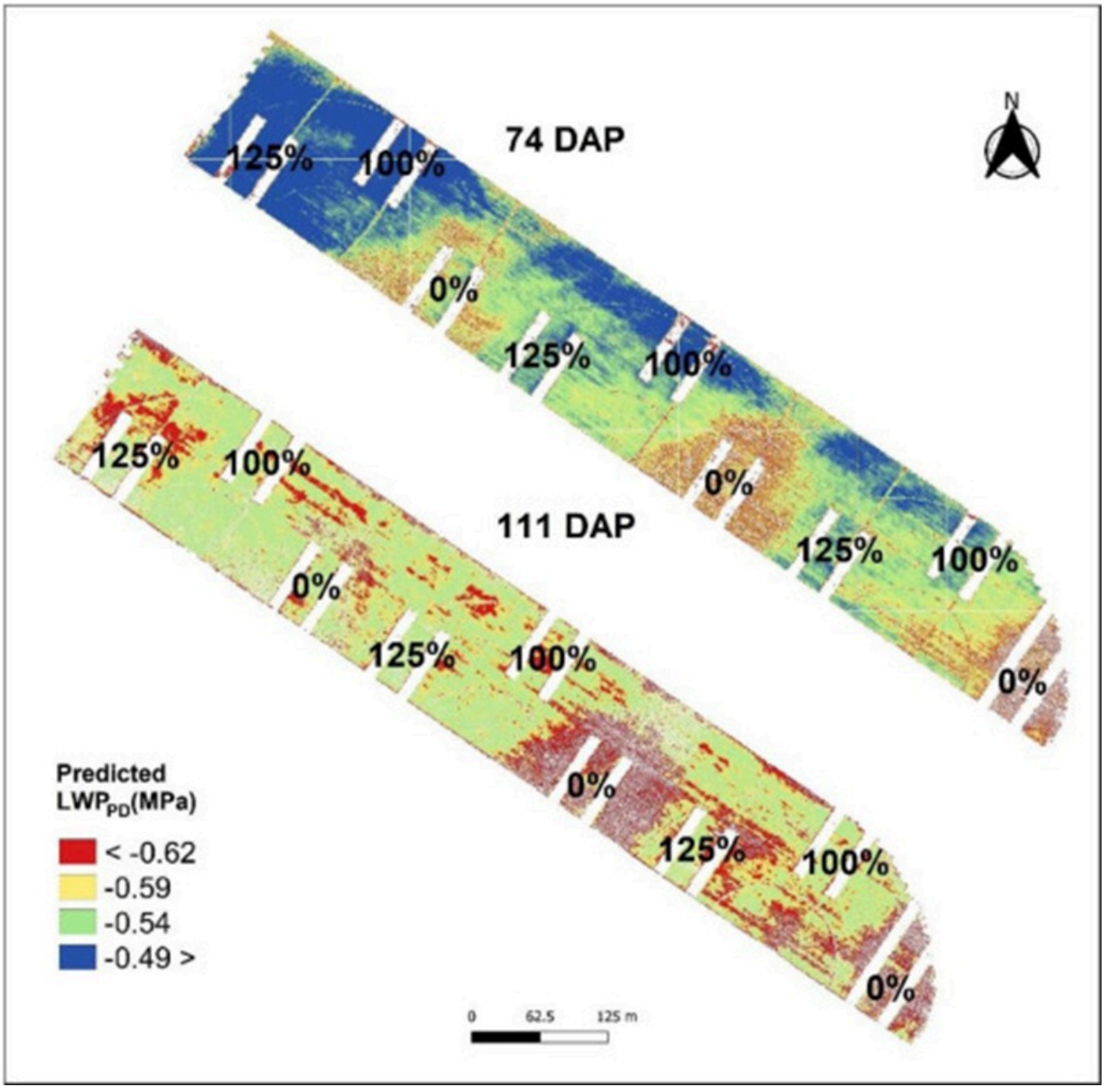

Figure 8. Predicted LWPPD maps based on the CWSIMonteith models developed at 74 DAP and 111 DAP in 2020.

The maps reveal that LWPPD variability observed in this study stemmed not solely from irrigation treatments but also from spatial differences in soil properties and water-holding capacity throughout the study field. Cohen *et al.* [55] emphasized the value of CWSI/LWP relationships for producing LWP maps throughout the season. Monitoring plant water

© 2025 The Author(s). | Published by Agro Intelligence Research Press

status via canopy temperature supports better irrigation management choices aligned with actual crop requirements, even in the southeastern US, where high humidity and frequent cloud cover complicate the approach [19]. This study's findings confirm that statement. Irrigation-driven water status patterns prove readily detectable within the field. On both dates, irrigated treatments showed higher predicted LWPPD than rainfed treatments. These contrasting patterns stood out more clearly at 74 DAP, when the color scale shifted from blue to red, with blue denoting the lowest and red the highest LWPPD values.

Conclusion

Findings of this study indicate that LWPPD values exceeding -0.45 MPa correspond to a non-stressed crop condition, with no adverse impacts on leaf stomatal conductance or crop growth noted, as evident throughout the 2018 growing season. In 2020, reduced and more erratic rainfall triggered notable variations in LAI and gs in addition to LWPPD. Irrigated treatments (well-irrigated and over-irrigated) generally exhibited higher LWPPD, LAI, and gs than rainfed treatments, indicating that drought stress imposed growth restrictions on non-irrigated plots. Sampling dates in the field did not align with times of maximum stress. Even though the season's lowest average LWPPD reached only -0.6 MPa, rainfed plots underwent roughly 17 days of prolonged drought while flowering. Despite these relatively elevated LWPPD readings, the various CWSIs maintained moderate to strong nonlinear associations with LWPPD, demonstrating that UAV-based thermal information can identify water-status patterns during milder drought conditions as well.

CWSI methods generated consistent outcomes over the 8 dates examined in both years. Although CWSIJones1 produced generally lower figures when calculated with theoretical wet and dry baselines, associations between all CWSIs and LWPPD displayed comparable R2 and RMSE. The strongest models appeared in 2020, showing moderate to relatively strong associations across all dates that year, with CWSIMonteith delivering the two highest R2 values among the 3 dates (0.65 and 0.58), paired with low RMSE values of 0.02 and 0.04 MPa, respectively.

In summary, outcomes highlighted the viability of an affordable UAV-thermal system for generating predicted LWP maps that accurately reflect existing field water conditions in the humid southeastern USA. Employing such maps allows growers to track variations in crop water status across the field throughout the season and supports more informed irrigation management decisions. Furthermore, these maps hold promise for creating dynamic variable-rate irrigation systems by defining crop-based in-season irrigation management zones.

Acknowledgements

This project was funded by the US-Israel Binational Agricultural Research and Development Fund (BARD) Research Project US-4991-1 and by the Georgia Agricultural Commodity Commission for Cotton Project No. 12-173GA-7. Special thanks to the University of Georgia's Stripling Irrigation Research Park and its staff for hosting and supporting the study.

Conflict of interest

None

Financial support

None

Ethics statement

None

© 2025 The Author(s). | Published by Agro Intelligence Research Press

Received: 11 Feb 2024 Revised: 17 Apr 2024 Accepted: 02 May 2024
Published online: 25 November 2025

Rights and permissions

Open Access The author(s) retain copyright. This article is licensed under the Creative Commons Attribution-NonCommercial-ShareAlike 4.0 International License. It may be shared and adapted for non-commercial purposes with appropriate attribution, an indication of changes, and distribution of adaptations under the same license. Third-party material may be subject to separate terms identified in its credit line. View the license at https://creativecommons.org/licenses/by-nc-sa/4.0/.

References

1. Chastain DR, Snider JL, Collins GD, Perry CD, Whitaker J, Byrd SA. Water deficit in field-grown Gossypium hirsutum primarily limits net photosynthesis by decreasing stomatal conductance, increasing photorespiration, and increasing the ratio of dark respiration to gross photosynthesis. J Plant Physiol. 171 (2014);1576–85. https://doi.org/10.1016/j.jplph.2014.07.014..

2. USDA. NASS- United States Department of Agriculture National Agricultural Statistics Service. https://www.nass.usda.gov/Statistics_by_Subject/, 2021 (accessed on 09 September 2021).

3. Feike T, Khor LY, Mamitimin Y, Ha N, Li L, Abdusalih N, et al. Determinants of cotton farmers' irrigation water management in arid Northwestern China. Agric Water Manag. 2017;187:1–10. https://doi.org/10.1016/j.agwat.2017.03.012..

4. Cetin O, Basbag S. Effects of climatic factors on cotton production in semi-arid regions: a review. Res Crops. 2010;11(3):785–91.

5. Constable GA, Bange MP. The yield potential of cotton (Gossypium hirsutum L.). Field Crops Res. 2015;182:98–106. https://doi.org/10.1016/j.fcr.2015.07.017..

6. Hearn AB. Water relationships in cotton. Outlook Agric. 1980;10(4):159–66. https://doi.org/10.1177/003072708001000402..

7. Turner NC, Hearn AB, Begg JE, Constable GA. Cotton (Gossypium hirsutum L.): physiological and morphological responses to water deficits and their relationship to yield. Field Crops Res. 1986;14:153–70. https://doi.org/10.1016/0378-4290(86)90054-7..

8. NOAA- National Oceanic and Atmospheric Administration. Climate monitoring. 2021. https://www.ncdc.noaa.gov/climate-monitoring/, (accessed on 09 July 2021).

9. Bednarz C, Ritchie G, Hook J, Yager R, Cromer S, Cook D, et al. Cotton crop water use and irrigation scheduling. In: Culpepper AS, editor. Georgia Cotton Research-Extension Report. Univ. of Georgia, Athens, GA, USA; 2002. p. 61–4.

10. Wang R, Zhang P, Meng Y, Wang Y, Chen B, Zhou Z. Drought effect on cotton yield and fiber quality on different fruiting branches. Crop Sci. 2016;56:1265–76. https://doi.org/10.2135/cropsci2015.08.0477..

11. Hu W, Snider JL, Wang H, Zhou Z, Chastain DR, Whitaker J, et al. Water-induced variation in yield and quality can be explained by altered yield component contributions in field-grown cotton. Field Crops Res. 2018;224:139–47. https://doi.org/10.1016/j.fcr.2018.05.013..

12. Loka DA, Oosterhuis DM, Ritchie GL. Water-deficit stress in cotton. In: Oosterhuis DM, editor. Stress physiology in cotton. The Cotton Foundation, Memphis, Tenn.; 2011. p. 37–72.

13. Yazar A, Sezen SM, Sesveren S. LEPA and trickle irrigation of cotton in the Southeast Anatolia Project (GAP) area in Turkey. Agric Water Manag. 2002;54(3):189–203. https://doi.org/10.1016/S0378-3774(01)00179-2..

14. Soth J, Grasser C, Salerno R. The impact of cotton on freshwater resources and ecosystems: a preliminary synthesis. Worldwide Fund for Nature, WWF, Gland, Switzerland; 1999.

15. Vellidis G, Liakos V, Andreis JH, Perry CD, Porter WM, Barnes EM, et al. Development and assessment of a smartphone application for irrigation scheduling in cotton. Comput Electron Agric. 2016;127:249–59. https://doi.org/10.1016/j.compag.2016.06.021..

16. Vellidis G, Liakos V, Porter W, Tucker M, Liang X. A dynamic variable rate irrigation control system. In: 13th International Conference on Precision Agriculture, St. Louis, Missouri; 2016.

17. Meeks CD, Snider JL, Porter WM, Vellidis G, Hawkins G, Rowland D. Assessing the utility of primed acclimation for improving water savings in cotton using a sensor-based irrigation scheduling system. Crop Sci. 2017;57(4):2117–29. https://doi.org/10.2135/cropsci2016.10.0907..

18. Li F, Dong Y, Zhao Y. Irrigation scheduling optimization for cotton based on the AquaCrop model. Water Resour Manag. 2019;33:39–55. https://doi.org/10.1007/s11269-018-2087-1..

19. Jones HG. Irrigation scheduling: advantages and pitfalls of plant-based methods. J Exp Bot. 2004;55:2427–36. https://doi.org/10.1093/jxb/erh213..

20. Grimes DW, Yamada H. Relation of cotton growth and yield to minimum leaf water potential. Crop Sci. 1982;22(1):134–9. https://doi.org/10.2135/cropsci1982.0011183X002200010031x..

21. Grimes DW, Yamada H, Hughes SW. Climate-normalized cotton leaf water potentials for irrigation scheduling. Agric Water Manag. 1987;12(4):293–304. https://doi.org/10.1016/0378-3774(87)90004-7..

22. Chastain DR, Snider JL, Collins GD, Perry CD, Whitaker J, Byrd SA, et al. Irrigation scheduling using predawn leaf water potential improves water productivity in drip-irrigated cotton. Crop Sci. 2016;56(6):3185–95. https://doi.org/10.2135/cropsci2016.01.0009..

23. Bellvert J, Zarco-Tejada PJ, Marsal J, Girona J, Gonzalez-Dugo V, Fereres E. Vineyard irrigation scheduling based on airborne thermal imagery and water potential thresholds. Aust J Grape Wine Res. 2016;22(2):307–15. https://doi.org/10.1111/ajgw.12173..

24. Paço TA, Ferreira MI, Pacheco CA. Scheduling peach orchard irrigation in water stress conditions: use of relative transpiration and predawn leaf water potential. Fruits. 2013;68(2):147–58. https://doi.org/10.1051/fruits/2013061..

25. Argyrokastritis IG, Papastylianou PT, Alexandris S. Leaf water potential and crop water stress index variation for full and deficit irrigated cotton in Mediterranean conditions. Agric Agric Sci Procedia. 2015;4:463–70. https://doi.org/10.1016/j.aaspro.2015.03.054..

26. Jackson RD. Canopy temperature and crop water stress. Adv Irrig. 1982;1:43–85. https://doi.org/10.1016/B978-0-12-024301-3.50009-5.

© 2025 The Author(s). | Published by Agro Intelligence Research Press

27. Elsayed S, Mistele B, Schmidhalter U. Can changes in leaf water potential be assessed spectrally? Funct Plant Biol. 2011;38:523–33. https://doi.org/10.1071/FP11021.

28. Alchanatis V, Cohen Y, Cohen S, Moller M, Sprinstin M, Meron M, et al. Evaluation of different approaches for estimating and mapping crop water status in cotton with thermal imaging. Precision Agric. 2010;11:27–41. https://doi.org/10.1007/s11119-009-9111-7.

29. Rosenberg O, Alchanatis V, Cohen Y. Are thermal images adequate for irrigation management? In: Stafford JV, editor. The 12th International Conference on Precision Agriculture, Sacramento, CA; 2014.

30. Cohen Y, Alchanatis V, Meron M, Saranga Y, Tsipris J. Estimation of leaf water potential by thermal imagery and spatial analysis. J Exp Bot. 2005;56(417):1843–52.

31. Cohen Y, Alchanatis V, Sela E, Saranga Y, Cohen S, Meron M, et al. Crop water status estimation using thermography: multi-year model development using ground-based thermal images. Precision Agric. 2015;16:311–29. https://doi.org/10.1007/s11119-014-9378-1.

32. Thomson SJ, Ouellet-Plamondon CM, DeFauw SL, Huang Y, Fisher DK, English PJ. Potential and challenges in use of thermal imaging for humid region irrigation system management. J Agric Sci. 2012;4(4):103. https://doi.org/10.5539/jas.v4n4p103.

33. Bodner G, Nakhforoosh A, Kaul HP. Management of crop water under drought: a review. Agron Sustain Dev. 2015;35:401–42. https://doi.org/10.1007/s13593-015-0283-4.

34. Jones HG, Serraj R, Loveys BR, Xiong L, Wheaton A, Price AH. Thermal infrared imaging of crop canopies for the remote diagnosis and quantification of plant responses to water stress in the field. Funct Plant Biol. 2009;36:978–89. https://doi.org/10.1071/FP09123.

35. Pennington DA, Heatherly L. Effects of changing solar radiation on canopy-air temperatures of cotton and soybeans. Agric For Meteorol. 1989;46:1–14. https://doi.org/10.1016/0168-1923(89)90108-1.

36. Meron M, Tsipris J, Orlov V, Alchanatis V, Cohen Y. Crop water stress mapping for site-specific irrigation by thermal imagery and artificial reference surfaces. Precision Agric. 2010;11:148–62. https://doi.org/10.1007/s11119-009-9153-x.

37. Gerhards M, Rock G, Schlerf M, Udelhoven T. Water stress detection in potato plants using leaf temperature, emissivity, and reflectance. Int J Appl Earth Obs Geoinf. 2016;53:27–39. https://doi.org/10.1016/j.jag.2016.08.004.

38. Idso SB, Jackson RD, Pinter JJ Jr, Reginato RJ, Hatfield JL. Normalizing the stress-degree-day parameter for environmental variability. Agric Meteorol. 1981;24:45–55. https://doi.org/10.1016/0002-1571(81)90032-7.

39. Jones HG. Use of infrared thermometry for estimation of stomatal conductance as a possible aid to irrigation scheduling. Agric For Meteorol. 1999;95(3):139–49. https://doi.org/10.1016/S0168-1923(99)00030-1.

40. Monteith JL, Unsworth ML. Principles of environmental physics. London, UK: Edward Arnold; 1990.

41. Ritchie GL, Whitaker JR, Bednarz CW, Hook JE. Subsurface drip and overhead irrigation: a comparison of plant boll distribution in upland cotton. Agron J. 2009;101(6):1336–44. https://doi.org/10.2134/agronj2009.0075.

© 2025 The Author(s). | Published by Agro Intelligence Research Press

42. Bauer P, Faircloth W, Rowland D, Richie G. Water sensitivity of cotton growth stages. In: Perry C, Barnes E, editors. Cotton irrigation management for humid regions. Cotton Incorporated; 2012.

43. Fisher DK. Simple and inexpensive lysimeters for monitoring reference- and crop-ET. Proceedings of the 25th Annual International Irrigation Conference, November 14–16, Tampa, Florida; 2004.

44. Snowden MC, Ritchie GL, Simao FR, Bordovsky JP. Timing of episodic drought can be critical in cotton. Crop Ecol Physiol. 2014;106(2):452–8. https://doi.org/10.2134/agronj2013.0325.

45. Zhang D, Luo Z, Liu S, Li W, Tang W, Dong H. Effects of deficit irrigation and plant density on the growth, yield and fiber quality of irrigated cotton. Field Crops Res. 2016;197:1–9. https://doi.org/10.1016/j.fcr.2016.06.003.

46. Noreen S, Athar HUR, Ashraf M. Interactive effects of watering regimes and exogenously applied osmoprotectants on earliness indices and leaf area index in cotton (Gossypium hirsutum L.) crop. Pak J Bot. 2013;45:1873–81.

47. Al-Khafaf S, Wierenga PJ, Williams BC. Evaporative flux from irrigated cotton as related to leaf area index, soil water, and evaporative demand. Agron J. 1978;70:912–7.

48. Saleem MF, Raza MAS, Ahmad S, Khan IH, Shahid AM. Understanding and mitigating the impacts of drought stress in cotton- a review. Pak J Bot. 2016;53(3):609–23.

49. Alves AAC, Setter TL. Response of cassava leaf area expansion to water deficit: cell proliferation, cell expansion and delayed development. Ann Bot. 2004;94(4):605–13.

50. Koch G, Rolland G, Dauzat M, Bédiée A, Baldazzi V, Bertin N, et al. Leaf production and expansion: A generalized response to drought stresses from cells to whole leaf biomass- A case study in the tomato compound leaf. Plants. 2019;8(10):409. https://doi.org/10.3390/plants8100409.

51. Tardieu F, Simonneau T. Variability among species of stomatal control under fluctuating soil water status and evaporative demand: modeling isohydric and anisohydric behaviors. J Exp Bot. 1998;49:419–32.

52. Li X, Smith R, Choat B, Tissue DT. Drought resistance of cotton (Gossypium hirsutum) is promoted by early stomatal closure and leaf shedding. Funct Plant Biol. 2020;47(2):91–8. https://doi.org/10.1071/FP19093.

53. Pilon C, Loka D, Snider JL, Oosterhuis DM. Drought-induced osmotic adjustment and changes in carbohydrate distribution in leaves and flowers of cotton (Gossypium hirsutum L.). J Agron Crop Sci. 2018;205(2):168–78. https://doi.org/10.1111/jac.12315.

54. O'Shaughnessy SA, Evett SR, Colaizzi PD, Howell TA. Using radiation thermography and thermometry to evaluate crop water stress in soybean and cotton. Agric Water Manag. 2011;98(10):1523–35. https://doi.org/10.1016/j.agwat.2011.05.005.

55. Cohen Y, Alchanatis V, Saranga Y, Rosenberg O, Sela E, Bosak A. Mapping water status based on aerial thermal imagery: comparison of methodologies for upscaling from a single leaf to commercial fields. Precision Agric. 2017;18:801–22. https://doi.org/10.1007/s11119-016-9484-3.

© 2025 The Author(s). | Published by Agro Intelligence Research Press